

Mass and star formation rate of the host galaxies of compact binary mergers across cosmic time

M. Celeste Artale^{1*}, Michela Mapelli^{1,2,3,4}, Yann Bouffanais², Nicola Giacobbo^{2,3,4}, Mario Spera^{1,2,3,4,5,6}, and Mario Pasquato^{3,4}

¹*Institut für Astro- und Teilchenphysik, Universität Innsbruck, Technikerstrasse 25/8, 6020 Innsbruck, Austria*

²*Physics and Astronomy Department Galileo Galilei, University of Padova, Vicolo dell'Osservatorio 3, I-35122, Padova, Italy*

³*INAF-Osservatorio Astronomico di Padova, Vicolo dell'Osservatorio 5, I-35122, Padova, Italy*

⁴*INFN-Padova, Via Marzolo 8, I-35131 Padova, Italy*

⁵*Center for Interdisciplinary Exploration and Research in Astrophysics (CIERA), Evanston, IL 60208, USA*

⁶*Department of Physics & Astronomy, Northwestern University, Evanston, IL 60208, USA*

14 October 2019

ABSTRACT

We investigate the properties of the host galaxies of compact binary mergers across cosmic time, by means of population-synthesis simulations combined with galaxy catalogues from the EAGLE suite. We analyze the merger rate per galaxy of binary neutron stars (BNSs), black hole–neutron star binaries (BHNSs) and binary black holes (BBHs) from redshift zero up to redshift six. The binary merger rate per galaxy strongly correlates with the stellar mass of the host galaxy at any redshift considered here. This correlation is significantly steeper for BNSs than for both BHNSs and BBHs. Moreover, we find that the merger rate per galaxy depends also on host galaxy’s star formation rate and metallicity. We derive a robust fitting formula that relates the merger rate per galaxy with galaxy’s star formation rate, stellar mass and metallicity at different redshifts. The typical masses of the host galaxies increase significantly as redshift decreases, as a consequence of the interplay between delay time distribution of compact binaries and cosmic assembly of galaxies. Finally, we study the evolution of the merger rate density with redshift. At low redshift ($z \leq 0.1$) early-type galaxies give a larger contribution to the merger rate density than late-type galaxies. This trend reverts at $z \geq 1$.

Key words: black hole physics – gravitational waves – methods: numerical – stars: black holes – stars: mass-loss

1 INTRODUCTION

The first and second observing runs (O1 and O2) of the LIGO-Virgo collaboration (LVC) led to the detection of ten binary black holes (BBHs) and one binary neutron star (BNS) (Abbott et al. 2016a,d,c, 2017a,c,b; Abbott & et al. 2018a,b), marking the dawn of gravitational-wave (GW) astronomy.

The third observing run (O3) started in April 2019, and several new gravitational-wave (GW) candidate triggers have already been released. By the end of O3, we expect to have a remarkable population of several tens of BBHs, several new BNSs, and possibly the first merging black hole – neutron star binaries (BHNSs).

KAGRA and LIGO–India will join the detector network soon (see e.g., Somiya 2012; Aso et al. 2013; Abbott et al.

2016b, 2018), while in about one decade from now third-generation ground-based GW detectors (Einstein Telescope and Cosmic Explorer) will lead to a dramatic improvement of sensitivity in GW searches and will be able to catch BBH mergers up to redshift $z \geq 10$ (see e.g. Punturo et al. 2010b,a; Sathyaprakash et al. 2012; Kalogera et al. 2019; GWIC-3G-SCT-Consortium 2019).

A population of several hundred merging compact objects would be a Rosetta stone to address long-standing open questions in astrophysics (Stevenson et al. 2015; Zevin et al. 2017; Fishbach et al. 2017; Fishbach et al. 2018; Wysocki et al. 2018; Bouffanais et al. 2019): it can provide a key to understand the evolution of massive binary stars (Bethe & Brown 1998; Belczynski et al. 2002; Dominik et al. 2013; Mennekens & Vanbeveren 2014; Spera et al. 2015; Belczynski et al. 2016; Marchant et al. 2016; Mandel & de Mink 2016; Eldridge & Stanway 2016; Stevenson et al. 2017; Chruslinska

* E-mail: Maria.Artale@uibk.ac.at, mcartale@gmail.com

et al. 2018; Kruckow et al. 2018; Spera et al. 2019; Mapelli et al. 2019; Eldridge et al. 2019; Giacobbo & Mapelli 2018, 2019), the formation channels of compact binaries (Portegies Zwart & McMillan 2000; Downing et al. 2010; Rodriguez et al. 2015, 2018; Askar et al. 2017; Samsing 2018; Samsing et al. 2018; Fragione & Kocsis 2018; Gerosa & Berti 2017; Antonini & Rasio 2016; Banerjee et al. 2010; Mapelli et al. 2013; Ziosi et al. 2014; Mapelli 2016; Banerjee 2017, 2018; Di Carlo et al. 2019; Bouffanais et al. 2019), and the role of primordial black holes as dark matter candidates (Carr & Hawking 1974; Carr et al. 2016; Bird et al. 2016; Sasaki et al. 2016; Clesse & García-Bellido 2017). Moreover, compact binary mergers can serve as standard sirens to estimate the Hubble constant (Schutz 1986; Abbott et al. 2017d; Chen et al. 2018; Vitale & Chen 2018; Fishbach et al. 2019; Soares-Santos et al. 2019; The LIGO Scientific Collaboration et al. 2019).

Identifying the host galaxies of GW sources is crucial, in order to better understand the astrophysical implications of these events. For example, host galaxy identification is pivotal to measure the Hubble constant (Fishbach et al. 2019; Gray et al. 2019) and gives important clues to reconstruct the formation channels of compact binaries (e.g. star clusters or field). So far, the host galaxy (NGC 4993) was identified only for the BNS merger GW170817 (Abbott et al. 2017e; Abbott et al. 2017f; Goldstein et al. 2017; Savchenko et al. 2017; Margutti et al. 2017; Coulter et al. 2017; Soares-Santos et al. 2017; Chornock et al. 2017; Cowperthwaite et al. 2017; Nicholl et al. 2017; Pian et al. 2017; Alexander et al. 2017).

Theoretical studies can give important contributions on the nature of host galaxies, eventually providing criteria to inform observational campaigns (see e.g., O’Shaughnessy et al. 2010; Dvorkin et al. 2016; Lamberts et al. 2016; Schneider et al. 2017; Cao et al. 2018; Mapelli et al. 2018; Mapelli & Giacobbo 2018; Artale et al. 2019; Marassi et al. 2019; Boco et al. 2019; Conselice et al. 2019; Mapelli et al. 2019). Previous work suggests that the merger rate of compact objects per galaxy in the local Universe strongly correlates with the stellar mass and star-formation rate (SFR) of the host galaxy (e.g., Mapelli et al. 2018; Cao et al. 2018; Artale et al. 2019). Moreover, the typical stellar mass of the host galaxies of BNSs might be significantly different from that of merging BBHs and BHNSs, especially at low redshift (Mapelli et al. 2018). This difference comes from the interplay between the distribution of delay times (i.e., the time between the formation of the stellar binary system and the merger event) and the dependence of BBH and BHNS merger efficiency on the metallicity of their progenitor stars (Mapelli et al. 2018; Toffano et al. 2019).

The host galaxies of merging compact objects can be also analysed in terms of early-type (ET) and late-type (LT) galaxies (O’Shaughnessy et al. 2010; Artale et al. 2019), which might help to disentangle the most likely places to detect GW events. Recently, Artale et al. (2019) proposed that ET galaxies host $\gtrsim 60$ per cent, $\gtrsim 64$ per cent, and $\gtrsim 73$ per cent of all the BNSs, BHNSs, and BBHs merging in the local Universe.

In this work, we characterize the host galaxies of merging compact binaries across cosmic time (up to redshift $z \sim 6$), by means of populations synthesis simulations (run with MOBSE, Giacobbo et al. 2018) combined with galaxy catalogues from the hydrodynamical cosmological simulation EAGLE (Schaye et al. 2015). We show that the merger rate per galaxy strongly

correlates with stellar mass, SFR and metallicity of the host galaxy, and we provide a simple fitting formula. These correlations mildly depend on redshift, tracing the evolution of the host galaxy population.

This paper is organized as follows. § 2 describes the main properties of EAGLE and MOBSE, and the methodology implemented to seed the EAGLE with a population of merging compact objects (BBHs, BNSs and BHNSs). We present our results in § 3. Our main conclusions are discussed in § 4.

2 METHOD

Following the same methodology originally introduced by Mapelli et al. (2017) (see also Mapelli et al. 2018; Mapelli & Giacobbo 2018; Mapelli et al. 2019; Artale et al. 2019), we combine the results from the population synthesis code MOBSE (Giacobbo et al. 2018) with the galaxy catalogues from the EAGLE simulation (Schaye et al. 2015). In this section we briefly describe the methodology; further details can be found in the aforementioned papers.

The population synthesis code MOBSE (Giacobbo et al. 2018) built from the BSE code (Hurley et al. 2000, 2002) includes new prescriptions for core collapse supernovae (SNe) based on Fryer et al. (2012), metallicity dependent stellar winds (see Vink et al. 2001; Vink & de Koter 2005; Chen et al. 2015), and pair-instability and pulsational pair-instability SNe (Woosley 2017; Spera & Mapelli 2017). Here we use the catalogue of merging compact objects from the run named as CC15 α 5 from Giacobbo & Mapelli (2018). This run was implemented also in Mapelli et al. (2018, 2019) and Artale et al. (2019). Run CC15 α 5 is composed of 12 sub-sets of metallicities $Z = 0.0002, 0.0004, 0.0008, 0.0012, 0.0016, 0.002, 0.004, 0.006, 0.008, 0.012, 0.016$ and 0.02 . Each sub-set was run with 10^7 stellar binaries, hence the total number of binary systems is 1.2×10^8 . For each merging compact binary, the MOBSE catalogue contains information about mass of the primary compact object, mass of the secondary compact object and delay time.

In this work we use galaxy catalogues of two runs from the EAGLE suite (Schaye et al. 2015; Crain et al. 2015). The EAGLE simulation, run with a modified version of the code GADGET-3, includes subgrid models to account for star formation, chemical enrichment, radiative cooling and heating, UV/X-ray ionizing background, stellar evolution, AGB stars and SN feedback, and AGN feedback.

We use the galaxy catalogue from the simulation REFL0100N1504 which represents a periodic box of 100 Mpc side (henceforth we refer to it as EAGLE100) with initially 1504^3 gas and dark matter particles. The initial mass of gas and dark matter particles is $m_{\text{gas}} = 1.81 \times 10^6 M_{\odot}$ and $m_{\text{DM}} = 9.70 \times 10^6 M_{\odot}$, respectively. In order to test the robustness of our results, we also use the run named RECALL0025N0752RUN, which represents a periodic box of 25 Mpc side (we refer to it as EAGLE25). EAGLE25 was run with the highest resolution in the EAGLE suite; it initially contains 752^3 gas and dark matter particles with $m_{\text{gas}} = 2.26 \times 10^5 M_{\odot}$ and $m_{\text{DM}} = 1.21 \times 10^6 M_{\odot}$. The two simulated boxes are complementary, since EAGLE25 has the highest resolution in the EAGLE suite (McAlpine et al. 2016), while EAGLE100 contains massive galaxies with stellar masses up to $1.9 \times 10^{12} M_{\odot}$. Hence, by comparing the results

of EAGLE25 and EAGLE100 we can estimate the robustness of our findings with respect to resolution and box-size related issues.

In the main text we discuss the results of EAGLE100 only. We present the results of EAGLE25 and compare them with EAGLE100 in Appendix A. We find very good agreement between the results we obtain with EAGLE100 and those with EAGLE25.

Information on the simulated galaxies is available on the SQL database¹. The EAGLE suite adopts the Λ CDM cosmology with parameters inferred from Planck Collaboration et al. (2014) ($\Omega_m = 0.2588$, $\Omega_\Lambda = 0.693$, $\Omega_b = 0.0482$, and $H_0 = 100 h \text{ km s}^{-1} \text{ Mpc}^{-1}$ with $h = 0.6777$). The simulation was run from $z = 127$ up to $z \sim 0$. From the database, we can extract the properties of the host galaxies (e.g. stellar mass M_* , SFR and metallicity of star-forming gas).

With a Monte Carlo algorithm, we assign a number of compact binaries (from MOBSE simulations) to each EAGLE stellar particle, based on its initial mass and metallicity. The formation time of compact-binary progenitors assigned to a given EAGLE particle is assumed to be the same as the formation time of the EAGLE particle. Each compact binary merges in the same stellar particle to which it was assigned (we do not allow for ejections of compact binaries) after its individual delay time (estimated from MOBSE). Following this procedure, we assign to each EAGLE galaxy a population of merging compact objects across cosmic time.

In this work, we study the host galaxies of BBHs, BHNSs, and BNSs at four representative redshift intervals: $z = 0 - 0.1$ (studied also in Artale et al. 2019), $z = 0.93 - 1.13$, $z = 1.87 - 2.12$, and $z = 5.73 - 6.51$. Hereafter, we will refer to these redshift intervals as $z = 0.1$, $z = 1$, $z = 2$ and $z = 6$ for brevity. The first interval ($z = 0.1$) is our local Universe sample, while $z = 1$ is representative of the advanced LIGO and Virgo horizon for BBHs at design sensitivity. Redshift $z = 2$ corresponds to the peak of star formation, while redshift $z = 6$ is approximately the end of the reionization epoch (we do not consider higher redshifts because the EAGLE does not include prescriptions for population III stars).

We select only galaxies with stellar mass above $10^7 M_\odot$ and $\text{SFR} > 0 M_\odot \text{ yr}^{-1}$. Hence, the catalogue from EAGLE100 has in total 77959, 91294, 116074, and 50544 galaxies at $z = 0.1, 1, 2$, and 6 , respectively. In the EAGLE25, we get 3070, 1827, 1806, and 412 galaxies at $z = 0.1, 1, 2$, and 6 , respectively.

3 RESULTS

3.1 Merger rate per galaxy

For each redshift interval, we calculate the number of BNSs, BHNSs and BBHs merging in each simulated galaxy. This number, divided by the considered time-span (1.84, 0.76, 0.41, and 0.14 Gyr for $z = 0.1, 1, 2$, and 6 , respectively), gives the merger rate per galaxy at a given redshift (n_{GW}). Artale et al. (2019) already computed this quantity for the local Universe, using the galaxy catalog from EAGLE25. Here, we extend their analysis to higher redshift ($z = 1, 2$ and 6) and using a larger simulated box.

We then performed a series of fits of increasing complexity and dimensionality that we refer to as Fit 1D, Fit 2D and Fit 3D, with the following prescriptions:

Fit 1D: we fit the merger rate per galaxy as a function of stellar mass (M_*) only, as

$$\log(n_{\text{GW}}/\text{Gyr}) = \alpha_1 \log(M_*/M_\odot) + \alpha_2. \quad (1)$$

Fit 2D: we fit the merger rate per galaxy as a function of both M_* and SFR, as

$$\begin{aligned} \log(n_{\text{GW}}/\text{Gyr}) = & \beta_1 \log(M_*/M_\odot) \\ & + \beta_2 \log(\text{SFR}/M_\odot \text{ yr}^{-1}) + \beta_3. \end{aligned} \quad (2)$$

Fit 3D: we fit the merger rate per galaxy as a function of M_* , SFR and metallicity Z , as

$$\begin{aligned} \log(n_{\text{GW}}/\text{Gyr}) = & \gamma_1 \log(M_*/M_\odot) \\ & + \gamma_2 \log(\text{SFR}/M_\odot \text{ yr}^{-1}) + \gamma_3 \log(Z) + \gamma_4. \end{aligned} \quad (3)$$

We adopted a standard linear regression approach using least-squares estimation to derive the values of the coefficients and their standard deviations. The results obtained are presented in Table 1, 2 and 3 for BNSs, BHNSs and BBHs respectively. These fits can help to identify the most likely host galaxies of merging compact objects according to their SFR, stellar mass and metallicity.

Figure 1 shows the evolution of the merger rate per galaxy as a function of the stellar mass at $z = 0.1, 1, 2$, and 6 , for BNS (left column), BHNS (middle column) and BBHs (right column). In all cases, we have a strong visual correlation between n_{GW} and the stellar mass of the host galaxy (in agreement with the correlation found by Artale et al. 2019, at $z \lesssim 0.1$), that is supported by Fit 1D represented by the red line on Figure 1. This correlation holds with relatively minor changes for all considered redshifts and is steeper for merging BNSs than for BBHs and BHNSs.

In addition, we find that adding the SFR and metallicity in Fit 2D and Fit 3D helped improve the quality of our fit. Quantitatively, we performed a simple model selection by computing the Bayesian Information Criterion (BIC) for all models (Schwarz 1978), and found that $\text{BIC}_{1\text{D}} > \text{BIC}_{2\text{D}} > \text{BIC}_{3\text{D}}$, indicating that the fit with more parameters is always preferred. It is worth mentioning that this behaviour is expected as the number of points used to do these fits is quite high and the dimensionality of our fits is low.

For the host galaxies of merging BBHs at $z = 0.1$, we find that the relation between the merger rate per galaxy and the stellar mass has a slight change in the slope at $\log(M_*/M_\odot) \sim 10.5$ (see Fig. 1). This is also seen but less significant at $z = 1$, and 2 . The trend is not present for the BNS hosts, and it is subtle for BHNS hosts.

The slope change for the host galaxies of merging BBHs is explained by the interplay between the mass-metallicity relation (MZR) of the galaxies and the strong dependence that BBH progenitors have on metallicity. Observational and numerical results have shown that the MZR is steep for galaxies with $M_* \sim 10^{8.5} - 10^{10.5} M_\odot$, with a turnover for $M_* > 10^{10.5} M_\odot$ (see e.g., Tremonti et al. 2004; Creasey et al. 2015). This is understood to be the result of the role that stellar feedback and AGN feedback have on the chemical evolution of galaxies. In particular the subgrid model from EAGLE suite (in both, EAGLE100 and EAGLE25) accounts for

¹ <http://icc.dur.ac.uk/Eagle/>, <http://virgo.dur.ac.uk/data.php>.

Table 1. Fits of the BNS merger rate per galaxy, from EAGLE100 at $z = 0.1, 1, 2,$ and 6 (see Sec. 3.1 for details).

		BNSs			
		$z = 0.1$	$z = 1$	$z = 2$	$z = 6$
Fit 1D	α_1	1.038 ± 0.001	1.109 ± 0.001	1.050 ± 0.001	1.027 ± 0.003
	α_2	-6.090 ± 0.010	-6.214 ± 0.006	-5.533 ± 0.006	-5.029 ± 0.021
Fit 2D	β_1	0.800 ± 0.002	0.964 ± 0.001	0.977 ± 0.001	1.113 ± 0.003
	β_2	0.323 ± 0.002	0.155 ± 0.001	0.068 ± 0.001	-0.070 ± 0.002
	β_3	-3.555 ± 0.018	-4.819 ± 0.013	-4.874 ± 0.011	-5.764 ± 0.026
Fit 3D	γ_1	0.701 ± 0.002	0.896 ± 0.002	1.018 ± 0.002	1.137 ± 0.004
	γ_2	0.356 ± 0.002	0.184 ± 0.001	0.048 ± 0.001	-0.082 ± 0.002
	γ_3	0.411 ± 0.005	0.222 ± 0.003	-0.103 ± 0.002	-0.053 ± 0.004
	γ_4	-1.968 ± 0.026	-3.795 ± 0.019	-5.451 ± 0.017	-6.104 ± 0.037

Table 2. Same as Table 1 but for BHNSs.

		BHNSs			
		$z = 0.1$	$z = 1$	$z = 2$	$z = 6$
Fit 1D	α_1	0.824 ± 0.001	0.873 ± 0.001	0.913 ± 0.001	0.965 ± 0.002
	α_2	-4.731 ± 0.008	-4.478 ± 0.008	-4.401 ± 0.007	-4.315 ± 0.018
Fit 2D	β_1	0.711 ± 0.002	0.813 ± 0.002	0.871 ± 0.002	0.985 ± 0.003
	β_2	0.150 ± 0.002	0.064 ± 0.002	0.039 ± 0.001	-0.017 ± 0.001
	β_3	-3.536 ± 0.016	-3.900 ± 0.018	-4.019 ± 0.014	-4.490 ± 0.024
Fit 3D	γ_1	0.833 ± 0.002	1.074 ± 0.002	1.084 ± 0.002	0.978 ± 0.003
	γ_2	0.101 ± 0.002	-0.058 ± 0.002	-0.068 ± 0.001	-0.013 ± 0.002
	γ_3	-0.461 ± 0.004	-0.788 ± 0.004	-0.535 ± 0.003	0.016 ± 0.004
	γ_4	-5.434 ± 0.022	-7.733 ± 0.023	-7.055 ± 0.018	-4.386 ± 0.034

Table 3. Same as Table 1 but for BBHs.

		BBHs			
		$z = 0.1$	$z = 1$	$z = 2$	$z = 6$
Fit 1D	α_1	0.807 ± 0.001	0.813 ± 0.001	0.831 ± 0.001	0.933 ± 0.004
	α_2	-4.310 ± 0.006	-3.845 ± 0.008	-3.600 ± 0.008	-4.190 ± 0.026
Fit 2D	β_1	0.812 ± 0.001	0.840 ± 0.002	0.858 ± 0.002	1.053 ± 0.004
	β_2	-0.006 ± 0.001	-0.029 ± 0.002	-0.026 ± 0.001	-0.098 ± 0.002
	β_3	-4.358 ± 0.013	-4.109 ± 0.018	-3.850 ± 0.015	-5.213 ± 0.034
Fit 3D	γ_1	0.921 ± 0.001	1.134 ± 0.002	1.135 ± 0.002	1.131 ± 0.005
	γ_2	-0.051 ± 0.001	-0.172 ± 0.002	-0.167 ± 0.001	-0.137 ± 0.002
	γ_3	-0.404 ± 0.003	-0.839 ± 0.004	-0.681 ± 0.003	-0.171 ± 0.005
	γ_4	-6.049 ± 0.018	-8.338 ± 0.024	-7.758 ± 0.020	-6.321 ± 0.047

these feedbacks and shows the turnover in the MZR (Segers et al. 2016). We quantify the change in the slope and provide more details in Appendix B.

3.2 Merger probability per a given host's stellar mass and SFR

For each redshift interval, we compute the merger probability in a given bin of host's stellar mass and SFR ($M_{*,i}, \text{SFR}_j$), as

$$d_{i,j}^X = \frac{N_{\text{GW},i,j}^X}{N_{\text{tot},\text{GW}}^X}, \quad (4)$$

where $N_{\text{GW},i,j}^X$ is the sum of all events of kind X (where $X = \text{BNSs, BHNSs or BBHs}$) occurring in galaxies with mass in the i th bin (between $M_{*,i} - \Delta M_*/2$ and $M_{*,i} + \Delta M_*/2$) and SFR in the j th bin (between $\text{SFR}_i - \Delta \text{SFR}/2$ and $\text{SFR}_i + \Delta \text{SFR}/2$) for a given time span. The normalization $N_{\text{tot},\text{GW}}^X$ corresponds to the total number of mergers in all the galaxies of the simulated box, in a given time-span. As a consequence, summing over all the bins yields $\sum_{i,j} d_{i,j}^X = 1$.

The merger probability accounts for two different facts: i) the dependence of the number of compact-binary mergers

on stellar mass and SFR of the host galaxy; ii) the fact that massive galaxies are less numerous than low-mass galaxies, manifested in the galaxy stellar mass function.

We note that the merger probability per a given host stellar mass and SFR can be interpreted as the probability of having a compact-binary merger for a given stellar mass and SFR. We stress that $d_{i,j}^X$ represents the merger probability in a given bin of SFRs and stellar masses: it must not be confused with the merger rate per galaxy (which is instead indicated as n_{GW} and is discussed in the previous Section 3.1).

Figures 2, 3 and 4 show the merger probability of BNSs, BBHs and BHNSs, respectively, as a function of stellar mass and SFR at $z = 0.1, 1, 2$ and 6. In each case we use a grid of 25×25 bins in the range of $\log(M_*/M_\odot) \in [7.0, 12.5]$ and $\log(\text{SFR}/M_\odot \text{ yr}^{-1}) \in [-5.5, 2.5]$. We find a strong correlation between merger probability, stellar mass and SFR. This correlation holds for both low and high redshift. In order to test the robustness of our results, we also computed the merger probability using the galaxy catalog from EAGLE25 finding good agreement between the two simulated boxes. We present the comparison in Appendix A.

Massive galaxies host progressively more compact-binary

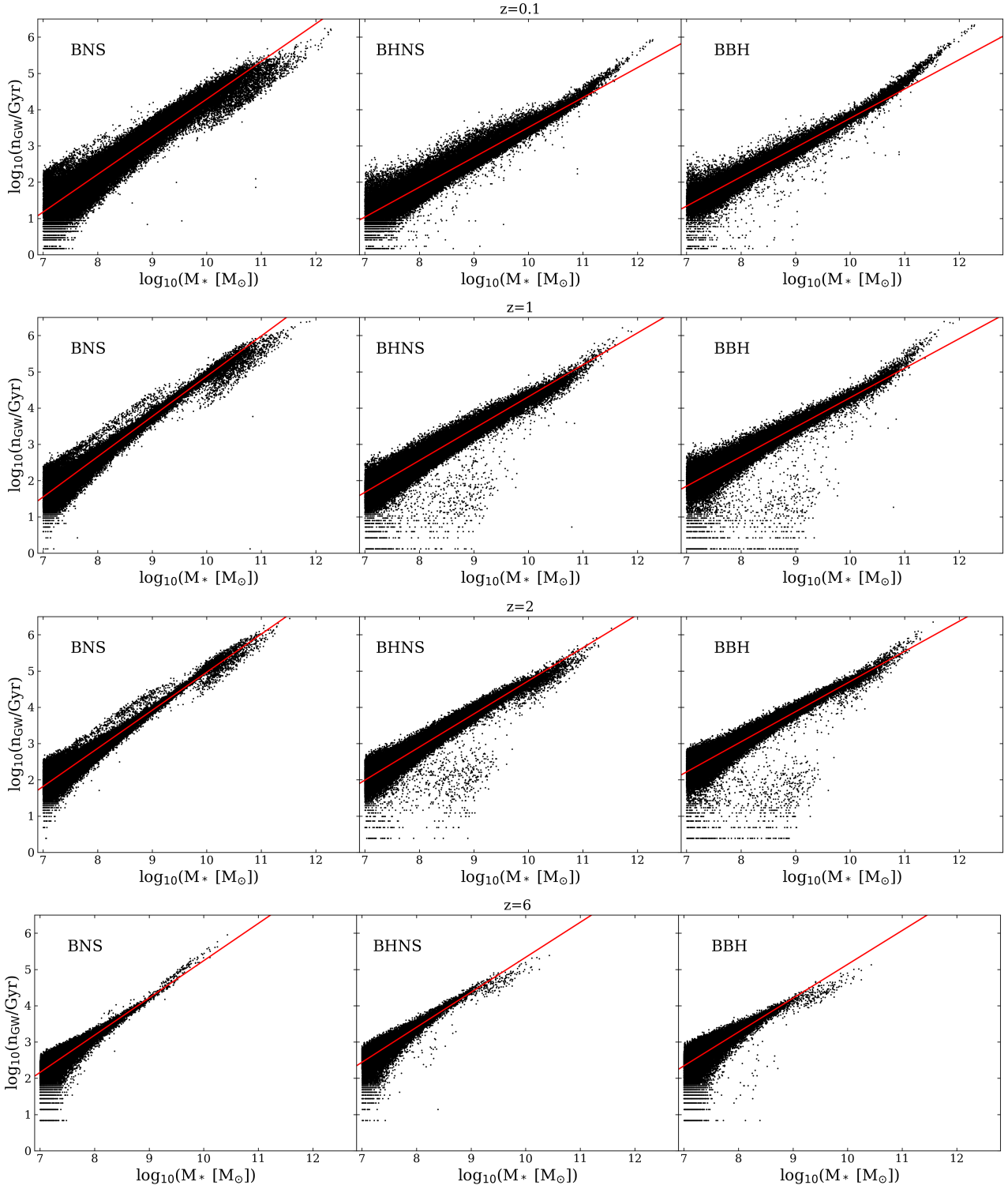


Figure 1. Merger rate per galaxy (n_{GW}) as a function of stellar mass M_* for the host galaxies of merging BNSs (left-hand panels), BHNSs (middle panels), and BBHs (right-hand panels), using EAGLE100. From top to bottom row: $z = 0.1$, $z = 1$, $z = 2$ and $z = 6$. Red lines: Fit 1D (see Tables 1, 2 and 3).

mergers as redshift decreases. This is apparent from the marginal histograms. To quantify the shift with redshift, we compute the median stellar mass from the marginal probability distributions. For merging BNSs, the median stellar masses of the hosts are $\log(M_*/M_{\odot}) = 10.4, 10.3, 10.2$, and

8.4 at $z = 0.1, 1, 2$, and 6 , respectively. For merging BHNSs, the median values are $\log(M_*/M_{\odot}) = 10.7, 10.2, 9.7$, and 8.0 , at $z = 0.1, 1, 2$, and 6 , respectively. Finally, for merging BBHs, the median stellar masses are $\log(M_*/M_{\odot}) = 10.9, 10.3, 9.8$, and 7.8 at $z = 0.1, 1, 2$, and 6 , respectively. This result is

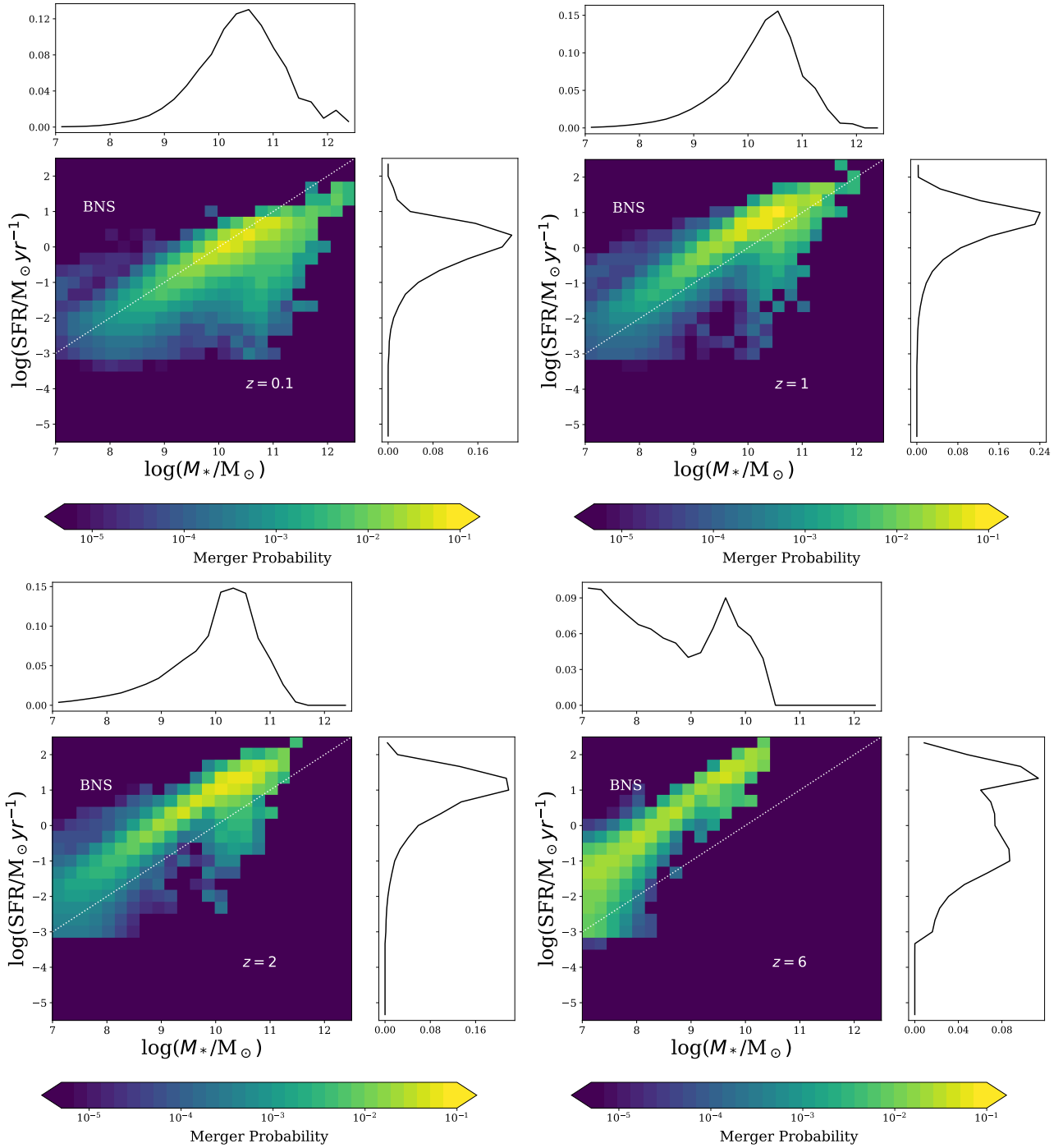


Figure 2. Merger probability per a given SFR and stellar mass (M_*) bin for BNSs, estimated from EAGLE100. The merger probability is calculated as described in equation 4. From top to bottom and from left to right: $z = 0.1$, $z = 1, 2$ and 6 . The white dotted line represents a specific SFR (sSFR) = 10^{-10} yr^{-1} . The marginal plots represent the distributions of SFR and M_* .

expected since galaxies grow and become more massive with time. The median of the stellar mass distribution for BBH hosts is shifted to a higher mass than for BNS, and BHNS hosts at $z = 0.1$, in agreement with previous works (Cao et al. 2018; Mapelli et al. 2018; Toffano et al. 2019). This trend is reversed at high redshift, where the median is larger for BNS hosts.

Finally, the host galaxy’s SFR strongly correlates with

M_* at every considered redshift. This is a consequence of the mass – SFR relation of galaxies (Furlong et al. 2015), as we already discussed in Artale et al. (2019). We also quantify the evolution of the SFR with redshift by computing median SFR from the marginal probability distributions. For merging BNSs, the medians are $\log(\text{SFR}/M_\odot \text{ yr}^{-1}) = 0.07, 0.72, 1.0$, and 0.02 at $z = 0.1, 1, 2$, and 6 , respectively. For merging BHNSs, we get $\log(\text{SFR}/M_\odot \text{ yr}^{-1}) = 0.09, 0.65, 0.63$, and

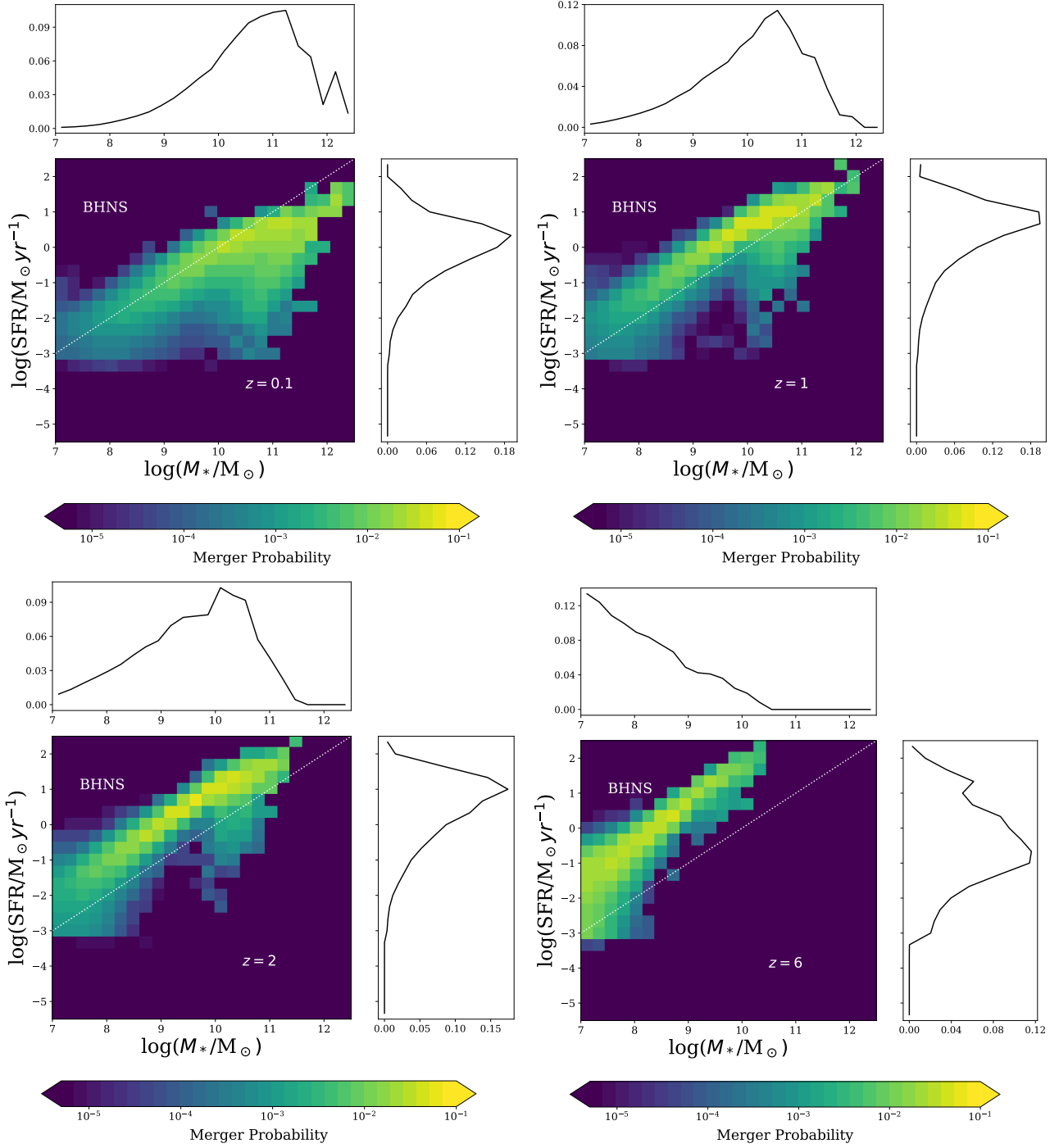


Figure 3. Same as Figure 2, but for BHNSs.

-0.46 at $z = 0.1, 1, 2$, and 6 , respectively. For merging BBHs, we obtain $\log(\text{SFR}/M_{\odot} \text{ yr}^{-1}) = 0.12, 0.65, 0.64$, and -0.69 at $z = 0.1, 1, 2$, and 6 , respectively. Our results show that the SFR medians reflect the evolution of the cosmic star formation rate in the Universe (Madau & Dickinson 2014), regardless of the kind of merging compact object.

3.3 Merger rate density evolution: early-type versus late-type host galaxies

Following Artale et al. (2019), we estimate the contribution to the merger rate density from early-type (R^{ET}) and late-type (R^{LT}) galaxies at $z = 0.1, 1, 2$, and 6 . We assume that galaxies with specific star formation rate (sSFR = SFR / M_{*}) lower than 10^{-10} yr^{-1} are early-type galaxies, while galaxies with $\text{sSFR} \geq 10^{-10} \text{ yr}^{-1}$ are late-type galaxies (see white dotted line in Fig. 2, 3, and 4 as reference).

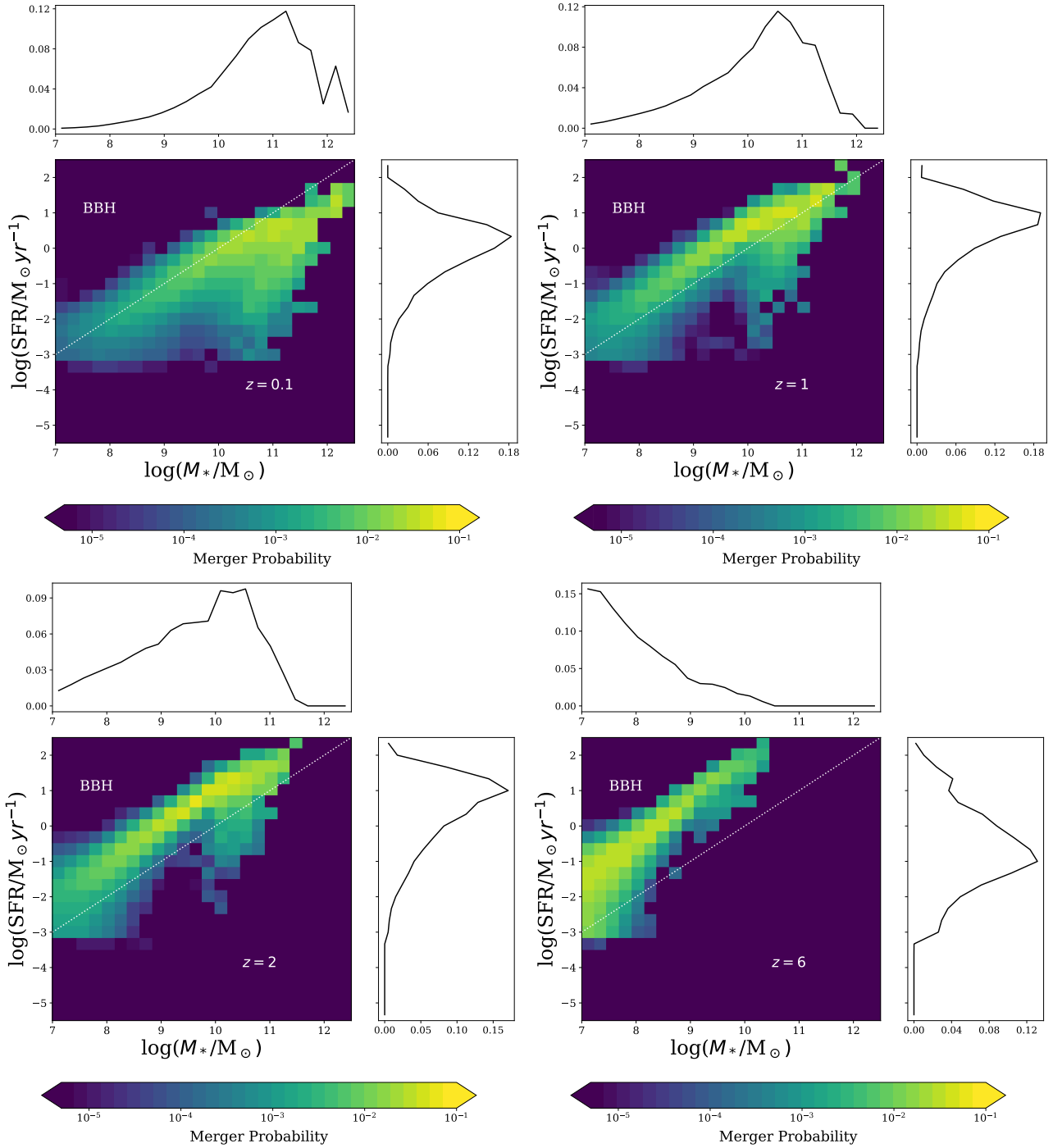


Figure 4. Same as Figure 2, but for BBHs.

We note that there is no general consensus about the definition of late-type and early-type galaxies at different redshifts (see e.g., Salim et al. 2007; Karim et al. 2011; Moustakas et al. 2013). Our choice to distinguish between late-type and early-type galaxies based on a sSFR threshold ($\text{sSFR} = 10^{-10} \text{ yr}^{-1}$) must be regarded as one of the simplest possible assumptions. Different choices do not affect our main results significantly.

Figure 5 shows the merger rate density of BNSs, BHNSs and BBHs as a function of redshift. We distinguish between

the contribution to the merger rate density from early-type galaxies and that from late-type galaxies. Early-type galaxies give a larger contribution to the merger rate density at $z \leq 0.1$ than late-type galaxies, in agreement with Artale et al. (2019). The trend reverts at higher redshifts ($z \geq 1$), where most mergers happen in late-type galaxies. This result springs from the combination of two effects. On the one hand, early-type galaxies become more and more common at low redshift, where they dominate the stellar mass budget (see e.g. Moffett et al. 2016). On the other hand, a large fraction of compact-

binary mergers in the local Universe are characterized by a long delay time (see e.g. Mapelli et al. 2018, 2019): these binary systems were born several Gyr ago in galaxies with high sSFR, but merge at low redshift in galaxies with low sSFR and large stellar mass.

4 CONCLUSIONS

We have characterized the host galaxies of compact-binary mergers across cosmic time, from redshift $z = 0$ to $z = 6$, by means of population-synthesis simulations run with the code MOBSE (Mapelli et al. 2017; Giacobbo et al. 2018), combined with galaxy catalogues from the EAGLE cosmological simulations.

We find that there is a strong correlation between the merger rate per galaxy n_{GW} and the stellar mass M_* of the host galaxy. This correlation holds at any redshifts considered here. We fit this correlation (Fit 1D) and we provide the best-fitting coefficients in Tables 1, 2 and 3 for BNSs, BHNSs and BBHs, respectively. The slope of the $n_{\text{GW}} - M_*$ correlation is steeper for BNSs than for both BHNSs and BBHs.

Moreover, we showed that including the SFR (Fit 2D) and the combination of SFR-metallicity (Fit 3D) improved the quality of our fit, especially in the latter case. This demonstrates that the merger rate per galaxy depends not only on M_* but also on SFR and Z . Hence, the merger rate per galaxy is maximum in galaxies with high mass, SFR and metallicity, both at low and high redshift (although galaxies are smaller at high z and thus the typical mass of the host galaxies decreases with z).

We have shown that our results do not depend significantly on the numerical resolution and on the box size of the cosmological simulation. Indeed, the correlations we find hold for both the EAGLE100 (a 100 Mpc of side comoving box simulation from the EAGLE suite) and the EAGLE25 (a 25 Mpc of side comoving box simulation from the EAGLE suite).

By studying the merger probability as a function of M_* and SFR (Figures 2, 3 and 4), we find that this quantity evolves significantly with redshift for all considered compact binaries (BNSs, BHNSs and BBHs). The merger probability accounts for the fact that massive galaxies have a large merger rate per galaxy, together with the galaxy stellar mass function showing that massive galaxies are less numerous than low mass galaxies.

At low redshift the merger probability shifts to higher stellar masses and to slightly lower SFR with respect to high redshift. This comes from the interplay between compact-binary delay time and cosmic evolution of the host galaxies. The typical stellar masses of the host galaxies shift to higher values at low redshift, because galaxies grow with time due to cosmic assembly: a large portion of the stellar mass at low redshift is locked into relatively massive galaxies (see e.g. Moffett et al. 2016). Moreover, star formation decreases from $z \sim 2$ to $z \sim 0$. In addition, only binary compact objects with short delay time are able to merge at high redshift, thus they tend to merge in the same galaxy where they formed (see e.g. Toffano et al. 2019). In contrast, at low redshift we have both compact binaries that merge with short delay time and compact binaries that formed at high redshift and merge at low redshift with long delay time. Binaries with a long delay time tend to merge in the most massive galaxies,

where they ended up after cosmic galaxy assembly (Mapelli et al. 2018).

Finally, we investigated the merger rate density of BNSs, BHNSs and BBHs (Figure 5). We distinguish between the contribution to the merger rate density from late-type and early-type galaxies. At low redshift ($z \leq 0.1$), the contribution to the merger rate from early-type galaxies is significantly larger than the one from late-type galaxies, while at higher redshift ($z \geq 1$) most mergers occur in late-type galaxies. This trend is a consequence of the interplay between cosmic galaxy assembly and the delay time distribution of the compact-object mergers.

Overall, our results predict a strong correlation between the merger rate and the properties (especially stellar mass and SFR) of host galaxies across cosmic time. Ongoing and future searches for electromagnetic counterparts of GW detections will probe this prediction, providing a fundamental test for compact-binary evolution models.

ACKNOWLEDGEMENT

We acknowledge the internal referee of LIGO-Virgo Giuseppe Greco for careful reading of the paper. MCA and MM acknowledge financial support from the Austrian National Science Foundation through FWF stand-alone grant P31154-N27 “Unraveling merging neutron stars and black hole – neutron star binaries with population synthesis simulations”. MM and YB acknowledge financial support by the European Research Council for the ERC Consolidator grant DEMOBLACK, under contract no. 770017. MS acknowledges funding from the European Union’s Horizon 2020 research and innovation programme under the Marie-Sklodowska-Curie grant agreement No. 794393. MP acknowledges funding from the European Union’s Horizon 2020 research and innovation programme under the Marie Skłodowska-Curie grant agreement No. 664931. We acknowledge the Virgo Consortium for making the EAGLE suite available. The EAGLE simulations were performed using the DiRAC-2 facility at Durham, managed by the ICC, and the PRACE facility Curie based in France at TGCC, CEA, Bruyères-le-Châtel.

REFERENCES

- Abbott B. P., et al. 2018b, preprint, ([arXiv:1811.12940](https://arxiv.org/abs/1811.12940))
- Abbott B. P., et al. 2018a, preprint, ([arXiv:1811.12907](https://arxiv.org/abs/1811.12907))
- Abbott B. P., et al., 2016a, Physical Review X, 6, 041015
- Abbott B. P., et al., 2016b, Living Reviews in Relativity, 19, 1
- Abbott B. P., et al., 2016c, Physical Review Letters, 116, 061102
- Abbott B. P., et al., 2016d, Physical Review Letters, 116, 241103
- Abbott B. P., et al., 2017a, Physical Review Letters, 118, 221101
- Abbott B. P., et al., 2017b, Physical Review Letters, 119, 141101
- Abbott B. P., et al., 2017c, Physical Review Letters, 119, 161101
- Abbott B. P., et al., 2017d, Nature, 551, 85
- Abbott B. P., et al., 2017e, ApJ, 848, L12
- Abbott B. P., et al., 2017f, The Astrophysical Journal Letters, 848, L13
- Abbott B. P., et al., 2018, Living Reviews in Relativity, 21, 3
- Alexander K. D., et al., 2017, The Astrophysical Journal Letters, 848, L21
- Ando T., 2010, Bayesian model selection and statistical modeling. Chapman and Hall/CRC
- Antonini F., Rasio F. A., 2016, ApJ, 831, 187

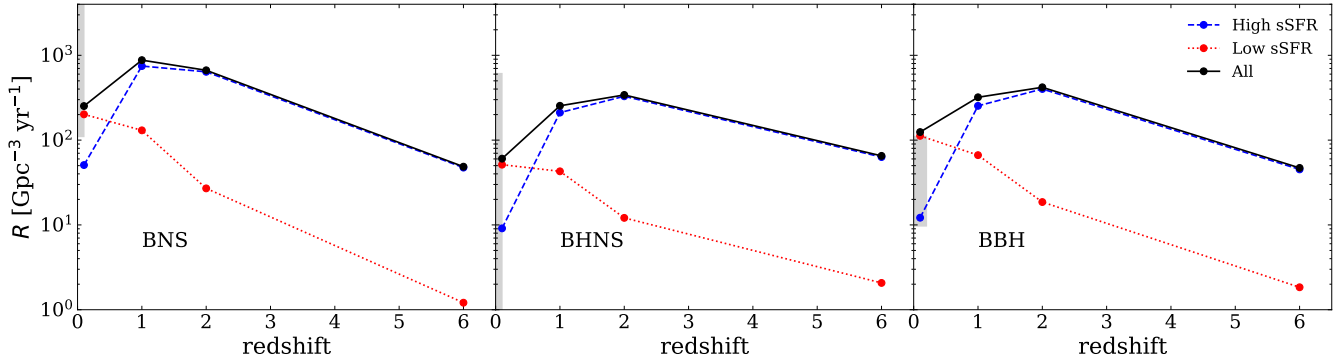


Figure 5. Merger rate density of BNSs (left-hand panel), BHNSs (middle panel) and BBHs (right-hand panel) as a function of redshift. Black circles and solid lines: total merger rate density; red circles and dotted lines: contribution to the merger rate density of early-type galaxies; blue circles and dashed lines: contribution to the merger rate density of late-type galaxies. Gray regions: merger rate densities within 90 % credible levels reported by the LIGO-Virgo collaboration (Abbott & et al. 2018a).

- Artale M. C., Mapelli M., Giacobbo N., Sabha N. B., Spera M., Santoliquido F., Bressan A., 2019, *MNRAS*, 487, 1675
- Askar A., Szkudlarek M., Gondek-Rosińska D., Giersz M., Bulik T., 2017, *MNRAS*, 464, L36
- Aso Y., Michimura Y., Somiya K., Ando M., Miyakawa O., Sekiguchi T., Tatsumi D., Yamamoto H., 2013, *Phys. Rev. D*, 88, 043007
- Banerjee S., 2017, *MNRAS*, 467, 524
- Banerjee S., 2018, *MNRAS*, 473, 909
- Banerjee S., Baumgardt H., Kroupa P., 2010, *MNRAS*, 402, 371
- Belczynski K., Kalogera V., Bulik T., 2002, *ApJ*, 572, 407
- Belczynski K., Holz D. E., Bulik T., O’Shaughnessy R., 2016, *Nature*, 534, 512
- Bethe H. A., Brown G. E., 1998, *ApJ*, 506, 780
- Bird S., Cholis I., Muñoz J. B., Ali-Haïmoud Y., Kamionkowski M., Kovetz E. D., Raccañelli A., Riess A. G., 2016, *Physical Review Letters*, 116, 201301
- Boco L., Lapi A., Goswami S., Perrotta F., Baccigalupi C., Danese L., 2019, *arXiv e-prints*, p. arXiv:1907.06841
- Bouffanais Y., Mapelli M., Gerosa D., Di Carlo U. N., Giacobbo N., Berti E., Baibhav V., 2019, *arXiv e-prints*,
- Cao L., Lu Y., Zhao Y., 2018, *MNRAS*, 474, 4997
- Carr B. J., Hawking S. W., 1974, *MNRAS*, 168, 399
- Carr B., Kühnel F., Sandstad M., 2016, *Phys. Rev. D*, 94, 083504
- Chen Y., Bressan A., Girardi L., Marigo P., Kong X., Lanza A., 2015, *MNRAS*, 452, 1068
- Chen H.-Y., Fishbach M., Holz D. E., 2018, *Nature*, 562, 545
- Chornock R., et al., 2017, *The Astrophysical Journal Letters*, 848, L19
- Chruslinska M., Belczynski K., Klencki J., Benacquista M., 2018, *MNRAS*, 474, 2937
- Clesse S., García-Bellido J., 2017, *Physics of the Dark Universe*, 15, 142
- Conselice C. J., Bhatavdekar R., Palmese A., Hartley W. G., 2019, *arXiv e-prints*, p. arXiv:1907.05361
- Coulter D. A., et al., 2017, *Science*, 358, 1556
- Cowperthwaite P. S., et al., 2017, *The Astrophysical Journal Letters*, 848, L17
- Crain R. A., et al., 2015, *MNRAS*, 450, 1937
- Creasey P., Theuns T., Bower R. G., 2015, *MNRAS*, 446, 2125
- De Rossi M. E., Bower R. G., Font A. S., Schaye J., Theuns T., 2017, *MNRAS*, 472, 3354
- Di Carlo U. N., Giacobbo N., Mapelli M., Pasquato M., Spera M., Wang L., Haardt F., 2019, *arXiv e-prints*,
- Dominik M., Belczynski K., Fryer C., Holz D. E., Berti E., Bulik T., Mandel I., O’Shaughnessy R., 2013, *ApJ*, 779, 72
- Downing J. M. B., Benacquista M. J., Giersz M., Spurzem R., 2010, *MNRAS*, 407, 1946
- Dvorkin I., Vangioni E., Silk J., Uzan J.-P., Olive K. A., 2016, *MNRAS*, 461, 3877
- Eldridge J. J., Stanway E. R., 2016, *MNRAS*, 462, 3302
- Eldridge J. J., Stanway E. R., Tang P. N., 2019, *MNRAS*, 482, 870
- Fishbach M., Holz D. E., Farr B., 2017, *ApJ*, 840, L24
- Fishbach M., Holz D. E., Farr W. M., 2018, *Astrophys. J.*, 863, L41
- Fishbach M., et al., 2019, *ApJ*, 871, L13
- Fragione G., Kocsis B., 2018, *Physical Review Letters*, 121, 161103
- Fryer C. L., Belczynski K., Wiktorowicz G., Dominik M., Kalogera V., Holz D. E., 2012, *ApJ*, 749, 91
- Furlong M., et al., 2015, *MNRAS*, 450, 4486
- GWIC-3G-SCT-Consortium 2019, *GWIC 3G Subcommittee Reports*
- Gerosa D., Berti E., 2017, *Phys. Rev.*, D95, 124046
- Giacobbo N., Mapelli M., 2018, *MNRAS*, 480, 2011
- Giacobbo N., Mapelli M., 2019, *MNRAS*, 482, 2234
- Giacobbo N., Mapelli M., Spera M., 2018, *MNRAS*, 474, 2959
- Goldstein A., et al., 2017, *ApJ*, 848, L14
- Gray R., et al., 2019, *arXiv e-prints*, p. arXiv:1908.06050
- Hurley J. R., Pols O. R., Tout C. A., 2000, *MNRAS*, 315, 543
- Hurley J. R., Tout C. A., Pols O. R., 2002, *MNRAS*, 329, 897
- Kalogera V., et al., 2019, in *Bulletin of the American Astronomical Society*. p. 242 (arXiv:1903.09220)
- Karim A., et al., 2011, *ApJ*, 730, 61
- Kruckow M. U., Tauris T. M., Langer N., Kramer M., Izzard R. G., 2018, *MNRAS*, 481, 1908
- Lamberts A., Garrison-Kimmel S., Clausen D. R., Hopkins P. F., 2016, *MNRAS*, 463, L31
- Madau P., Dickinson M., 2014, *ARA&A*, 52, 415
- Mandel I., de Mink S. E., 2016, *MNRAS*, 458, 2634
- Mapelli M., 2016, *MNRAS*, 459, 3432
- Mapelli M., Giacobbo N., 2018, *MNRAS*, 479, 4391
- Mapelli M., Zampieri L., Ripamonti E., Bressan A., 2013, *MNRAS*, 429, 2298
- Mapelli M., Giacobbo N., Ripamonti E., Spera M., 2017, *MNRAS*, 472, 2422
- Mapelli M., Giacobbo N., Toffano M., Ripamonti E., Bressan A., Spera M., Branchesi M., 2018, *MNRAS*, 481, 5324
- Mapelli M., Giacobbo N., Santoliquido F., Artale M. C., 2019, *MNRAS*, 487, 2
- Marassi S., Graziani L., Ginolfi M., Schneider R., Mapelli M., Spera M., Alparone M., 2019, *MNRAS*, 484, 3219

Marchant P., Langer N., Podsiadlowski P., Tauris T. M., Moriya T. J., 2016, *A&A*, 588, A50

Margutti R., et al., 2017, *The Astrophysical Journal Letters*, 848, L20

McAlpine S., et al., 2016, *Astronomy and Computing*, 15, 72

Mennekens N., Vanbeveren D., 2014, *A&A*, 564, A134

Moffett A. J., et al., 2016, *MNRAS*, 462, 4336

Moustakas J., et al., 2013, *ApJ*, 767, 50

Nicholl M., et al., 2017, *The Astrophysical Journal Letters*, 848, L18

O’Shaughnessy R., Kalogera V., Belczynski K., 2010, *ApJ*, 716, 615

Pian E., et al., 2017, *Nature*, 551, 67

Planck Collaboration et al., 2014, *A&A*, 571, A16

Portegies Zwart S. F., McMillan S. L. W., 2000, *ApJ*, 528, L17

Punturo M., et al., 2010a, *Classical and Quantum Gravity*, 27, 084007

Punturo M., et al., 2010b, *Classical and Quantum Gravity*, 27, 194002

Rodriguez C. L., Morscher M., Pattabiraman B., Chatterjee S., Haster C.-J., Rasio F. A., 2015, *Physical Review Letters*, 115, 051101

Rodriguez C. L., Amaro-Seoane P., Chatterjee S., Kremer K., Rasio F. A., Samsing J., Ye C. S., Zevin M., 2018, preprint, ([arXiv:1811.04926](https://arxiv.org/abs/1811.04926))

Salim S., et al., 2007, *ApJS*, 173, 267

Samsing J., 2018, *Phys. Rev. D*, 97, 103014

Samsing J., Askar A., Giersz M., 2018, *ApJ*, 855, 124

Sasaki M., Suyama T., Tanaka T., Yokoyama S., 2016, *Physical Review Letters*, 117, 061101

Sathyaprakash B., et al., 2012, *Classical and Quantum Gravity*, 29, 124013

Savchenko V., et al., 2017, *The Astrophysical Journal Letters*, 848, L15

Schaye J., et al., 2015, *MNRAS*, 446, 521

Schneider R., Graziani L., Marassi S., Spera M., Mapelli M., Alparone M., Bannassuti M. d., 2017, *MNRAS*, 471, L105

Schutz B. F., 1986, *Nature*, 323, 310

Schwarz G., 1978, *Ann. Statist.*, 6, 461

Segers M. C., Crain R. A., Schaye J., Bower R. G., Furlong M., Schaller M., Theuns T., 2016, *MNRAS*, 456, 1235

Soares-Santos M., et al., 2017, *The Astrophysical Journal Letters*, 848, L16

Soares-Santos M., et al., 2019, *ApJ*, 876, L7

Somiya K., 2012, *Classical and Quantum Gravity*, 29, 124007

Spera M., Mapelli M., 2017, *MNRAS*, 470, 4739

Spera M., Mapelli M., Bressan A., 2015, *MNRAS*, 451, 4086

Spera M., Mapelli M., Giacobbo N., Trani A. A., Bressan A., Costa G., 2019, *MNRAS*, 485, 889

Stevenson S., Ohme F., Fairhurst S., 2015, *ApJ*, 810, 58

Stevenson S., Vigna-Gómez A., Mandel I., Barrett J. W., Neijssel C. J., Perkins D., de Mink S. E., 2017, *Nature Communications*, 8, 14906

The LIGO Scientific Collaboration the Virgo Collaboration et al. 2019, arXiv e-prints, p. [arXiv:1908.06060](https://arxiv.org/abs/1908.06060)

Toffano M., Mapelli M., Giacobbo N., Artale M. C., Ghirlanda G., 2019, arXiv e-prints,

Tremonti C. A., et al., 2004, *ApJ*, 613, 898

Vink J. S., de Koter A., 2005, *A&A*, 442, 587

Vink J. S., de Koter A., Lamers H. J. G. L. M., 2001, *A&A*, 369, 574

Vitale S., Chen H.-Y., 2018, *Phys. Rev. Lett.*, 121, 021303

Woosley S. E., 2017, *ApJ*, 836, 244

Wysocki D., Gerosa D., O’Shaughnessy R., Belczynski K., Gladysz W., Berti E., Kesden M., Holz D. E., 2018, *Phys. Rev. D*, 97, 043014

Zevin M., Pankow C., Rodriguez C. L., Sampson L., Chase E., Kalogera V., Rasio F. A., 2017, *ApJ*, 846, 82

Ziosi B. M., Mapelli M., Branchesi M., Tormen G., 2014, *MNRAS*, 441, 3703

APPENDIX A: COMPARISON OF EAGLE25 AND EAGLE100

In the main text, we have discussed the results we obtained from EAGLE100, which represents the largest simulated box from the EAGLE suite. To test how robust our results are in terms of resolution and box size, we perform the same analysis using EAGLE25. The EAGLE25 simulation has a smaller box, but with a larger resolution than EAGLE100 (gas particles are ~ 8 times smaller in EAGLE25).

Figures A1, A2 and A3 show the merger probability density for merging BNSs, BHNSs and BBHs, respectively, as a function of the stellar mass and SFR of the host galaxies. We bin the stellar mass and SFR using the same binning that we used for EAGLE100. We find that the merger rates obtained with EAGLE25 are similar to those derived from EAGLE100. We note however that EAGLE25 does not have massive clusters, due to the size of the simulated box. Tables A1, A2 and A3 show the results of the fits proposed in Sec. 3.1. Our results show that the coefficients of Fit 1D for EAGLE100 and EAGLE25 are in good agreement, with percentage errors smaller than $\sim 8\%$. This again indicates that the stellar mass of host galaxies of merging compact objects is a crucial property to trace their merger rates. For Fits 2D and 3D, we also find agreement between the two galaxy catalogues, with only few cases showing large discrepancies with percentage errors of the coefficients standing above $\sim 20\%$. It is worth mentioning that only the coefficients attached to SFR and metallicity are concerned. This is expected, because SFR and metallicity are more affected by simulation resolution and box size, as they strongly depend on sub-grid prescriptions (see e.g., Furlong et al. 2015; De Rossi et al. 2017).

APPENDIX B: CHANGE OF SLOPE IN THE $N_{\text{GW}} - M_*$ CORRELATION

From a visual inspection of Figure 1, it appears that there is a subtle change of the slope of BBH hosts galaxies at $\log(M_*/M_\odot) \sim 10.5$ for redshift $z = 0.1, 1$ and 2. This trend does not appear in BNS hosts, and is less clear for BHNS hosts.

We measure how significant the slope change is, by using two different (but related) methods. First, based on Fit 1D from Sec. 3.1, we perform an ordinary least squares regression for the two following models (where M_* is taken in units of M_\odot , $\theta(x)$ is the Heaviside step function, and ϵ represents an independent, identically distributed noise term):

$$\text{BBH} = a \log(M_*) + b + \epsilon \quad (\text{B1})$$

and

$$\text{BBH} = a \log(M_*) + b + c\theta(\log(M_*) - 10.5) \log(M_*) + \epsilon. \quad (\text{B2})$$

For the latter fit we obtain that the c coefficient is significant to $p < 2 \cdot 10^{-16}$, corresponding to a value of the t statistic of 59. We also use the Bayesian Information Criterion (BIC) to compare the goodness of the fit for the two models. The BIC can be interpreted as a penalized log-likelihood of the model,

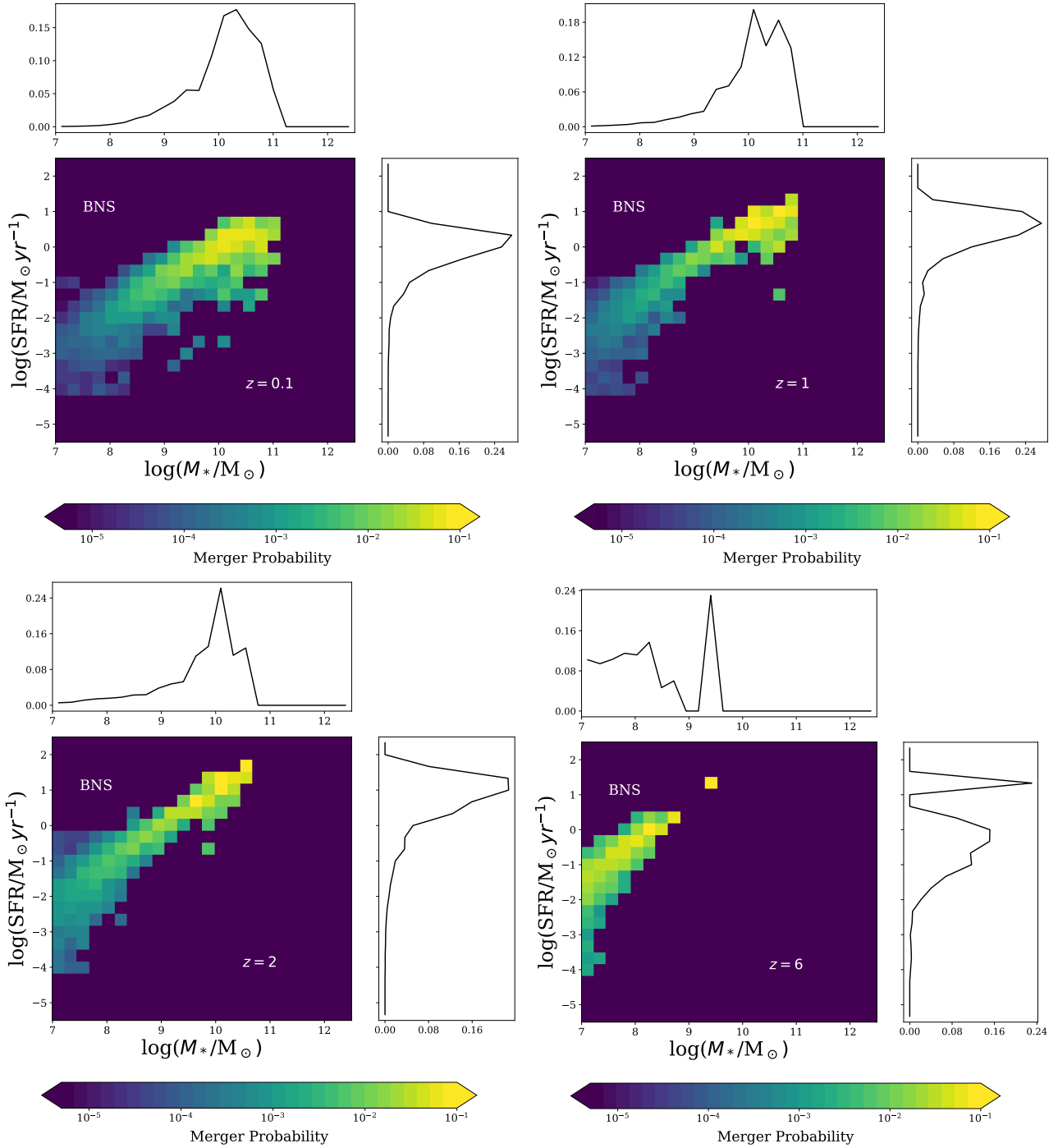


Figure A1. Merger probability for BNSs at redshifts $z = 0.1, 1, 2$ and 6 as a function of the stellar mass and SFR for the EAGLE25 galaxy catalogue. Marginal histograms represent the distributions of SFR and M_* .

where the penalty term takes into account the number of free parameters (Ando 2010). The more negative the BIC is, the better is the model. We find $\text{BIC} = -46089$ for the first model (without slope change), while $\text{BIC} = -49479$ for the second model with slope change, which is unsurprisingly aligned with our results based on the adjusted R-squared.

The slope change of the host galaxies of BBH mergers arises from the interplay between the MZR and the strong dependence on metallicity of BBH progenitors. In fact, the MZR

is steep for galaxies with $M_* \sim 10^{8.5} - 10^{10.5} M_\odot$, but has a turnover for masses above $10^{10.5} M_\odot$ (see e.g., Tremonti et al. 2004; Creasey et al. 2015; Segers et al. 2016). This results from the efficiency of different feedback mechanisms: stellar feedback is the dominant effect in low-mass galaxies, while AGN feedback is the dominant effect for $M_* > 10^{10.5} M_\odot$.

As a consequence of AGN feedback, galaxies above $10^{10.5} M_\odot$ host stars with a slightly lower metallicity than smaller galaxies, and thus host BBH mergers more efficiently.

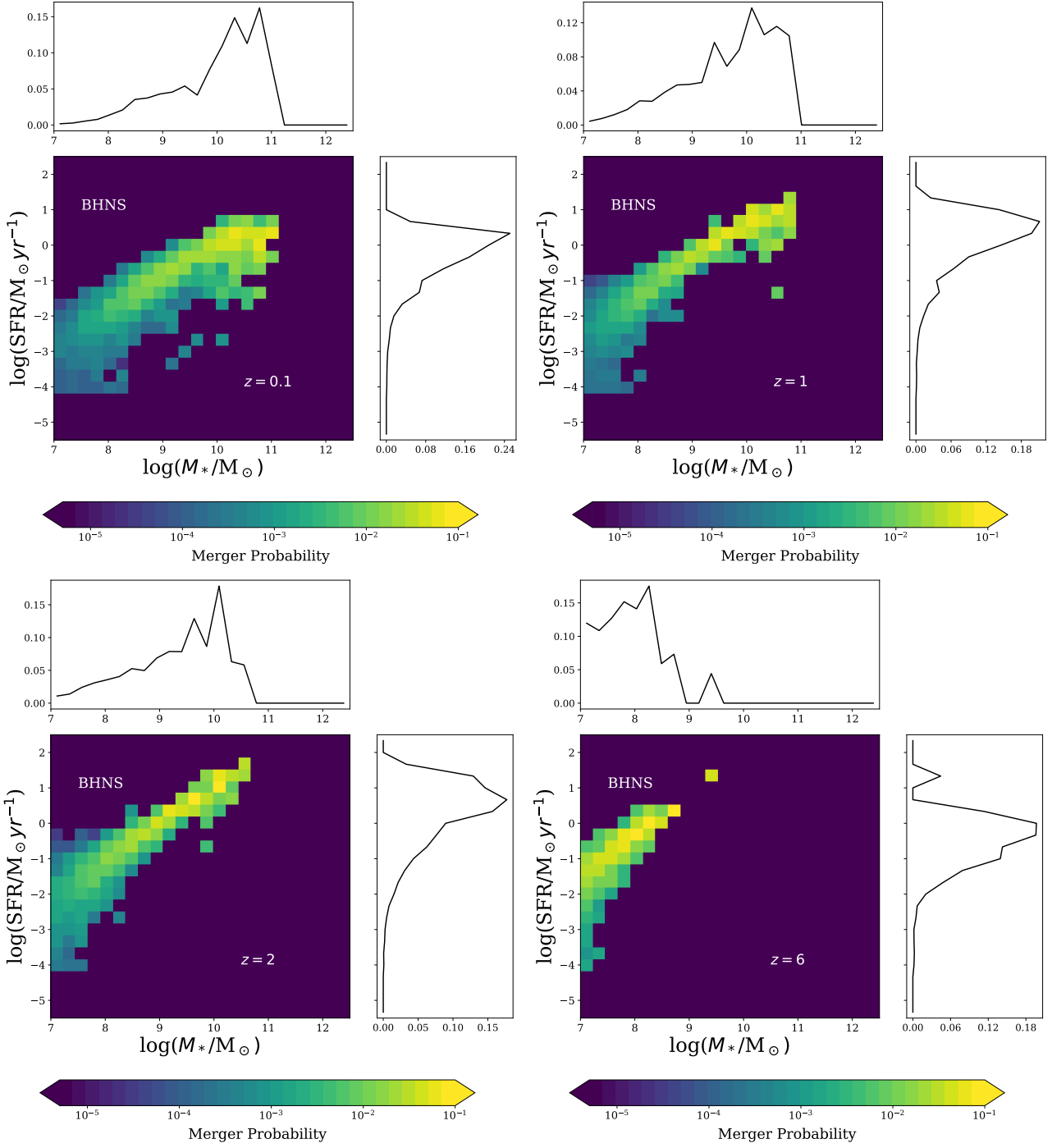


Figure A2. Same as Figure A1 but for BHNSs.

This in turn produces a higher number of merging BBHs in the local Universe, increasing the merger rate per galaxy, n_{GW} .

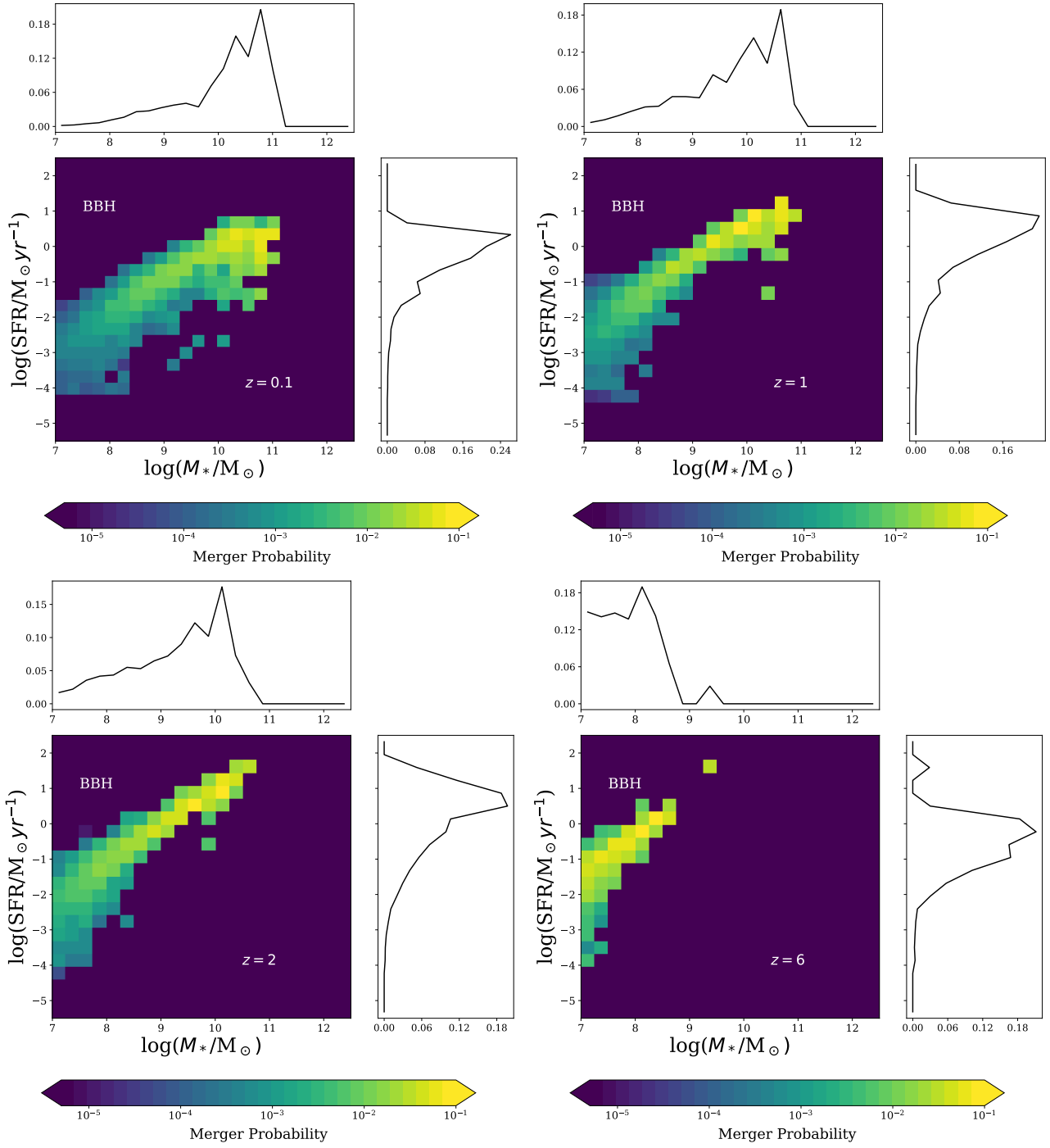


Figure A3. Same as Figure A1 but for BBHs.

Table A1. Same as Table 1 for BNSs, but using EAGLE25.

		BNSs			
		$z = 0.1$	$z = 1$	$z = 2$	$z = 6$
Fit 1D	α_1	1.073 ± 0.005	1.083 ± 0.005	0.992 ± 0.006	0.999 ± 0.017
	α_2	-6.512 ± 0.046	-6.165 ± 0.039	-5.099 ± 0.044	-4.886 ± 0.130
Fit 2D	β_1	0.865 ± 0.010	1.025 ± 0.010	0.960 ± 0.010	1.021 ± 0.025
	β_2	0.217 ± 0.009	0.053 ± 0.008	0.026 ± 0.007	-0.016 ± 0.013
	β_3	-4.392 ± 0.096	-5.618 ± 0.090	-4.816 ± 0.089	-5.073 ± 0.199
Fit 3D	γ_1	0.852 ± 0.015	1.096 ± 0.015	1.076 ± 0.016	1.054 ± 0.037
	γ_2	0.225 ± 0.011	0.014 ± 0.010	-0.029 ± 0.009	-0.033 ± 0.020
	γ_3	0.031 ± 0.027	-0.136 ± 0.022	-0.235 ± 0.025	-0.067 ± 0.057
	γ_4	-4.214 ± 0.182	-6.553 ± 0.179	-6.386 ± 0.189	-5.524 ± 0.434

Table A2. Same as Table 2 for BHNSs but using EAGLE25.

		BHNSs			
		$z = 0.1$	$z = 1$	$z = 2$	$z = 6$
Fit 1D	α_1	0.820 ± 0.007	0.850 ± 0.008	0.915 ± 0.006	1.012 ± 0.015
	α_2	-4.510 ± 0.058	-4.149 ± 0.062	-4.357 ± 0.047	-4.726 ± 0.114
Fit 2D	β_1	0.604 ± 0.013	0.719 ± 0.016	0.860 ± 0.011	0.976 ± 0.022
	β_2	0.224 ± 0.012	0.120 ± 0.012	0.046 ± 0.008	0.026 ± 0.011
	β_3	-2.318 ± 0.127	-2.907 ± 0.142	-3.863 ± 0.094	-4.423 ± 0.174
Fit 3D	γ_1	1.011 ± 0.016	1.171 ± 0.020	1.154 ± 0.0143	0.990 ± 0.033
	γ_2	-0.031 ± 0.012	-0.123 ± 0.013	-0.096 ± 0.008	0.019 ± 0.017
	γ_3	-0.994 ± 0.028	-0.874 ± 0.029	-0.598 ± 0.023	-0.029 ± 0.050
	γ_4	-8.036 ± 0.193	-8.863 ± 0.230	-7.862 ± 0.171	-4.619 ± 0.379

Table A3. Same as Table 3 for BBHs but using EAGLE25.

		BBHs			
		$z = 0.1$	$z = 1$	$z = 2$	$z = 6$
Fit 1D	α_1	0.792 ± 0.006	0.792 ± 0.008	0.838 ± 0.007	0.918 ± 0.019
	α_2	-4.059 ± 0.046	-3.504 ± 0.061	-3.537 ± 0.053	-4.086 ± 0.139
Fit 2D	β_1	0.700 ± 0.011	0.728 ± 0.016	0.850 ± 0.012	0.966 ± 0.027
	β_2	0.095 ± 0.010	0.058 ± 0.013	-0.010 ± 0.009	-0.034 ± 0.014
	β_3	-3.124 ± 0.108	-2.905 ± 0.145	-3.639 ± 0.108	-4.482 ± 0.212
Fit 3D	γ_1	0.993 ± 0.015	1.167 ± 0.020	1.234 ± 0.015	1.096 ± 0.039
	γ_2	-0.090 ± 0.011	-0.176 ± 0.013	-0.196 ± 0.009	-0.104 ± 0.020
	γ_3	-0.699 ± 0.027	-0.851 ± 0.031	-0.782 ± 0.024	-0.269 ± 0.059
	γ_4	-7.211 ± 0.182	-8.684 ± 0.238	-8.867 ± 0.180	-6.305 ± 0.451